Available online at www.sciencedirect.com
SCIENCE DIRECT
Earth and Planetary Science Letters 247 (2006) 41–60
EPSL
www.elsevier.com/locate/epsl

Precessional forcing of lacustrine sedimentation in the late Cenozoic Chemeron Basin, Central Kenya Rift, and calibration of the Gauss/Matuyama boundary

Alan L. Deino [a,*], John D. Kingston [b], Jonathan M. Glen [a,c], Robert K. Edgar [d], Andrew Hill [e]

[a] *Berkeley Geochronology Center, 2455 Ridge Road, Berkeley, CA 94709, USA*
[b] *Department of Anthropology, Emory University, Atlanta, GA 30322, USA*
[c] *US Geological Survey, MS989, 345 Middlefield Road, Menlo Park, CA 94025, USA*
[d] *Farlow Herbarium of Cryptogamic Botany, Harvard University, Cambridge, MA 02138, USA*
[e] *Department of Anthropology, Yale University, New Haven, CT 06520, USA*

Received 15 November 2005; received in revised form 22 March 2006; accepted 6 April 2006

Editor: V. Courtillot

Abstract

The fluviolacustrine sedimentary sequence of the Chemeron Formation exposed in the Barsemoi River drainage, Tugen Hills, Kenya, contains a package of five successive diatomite/fluvial cycles that record the periodic development of freshwater lakes within the axial portion of the Central Kenya Rift. The overwhelming abundance in the diatomite of planktonic species of the genera *Aulacoseira* and *Stephanodiscus*, and the virtual absence of benthic littoral diatoms and detrital material indicate areally extensive, deep lake systems. A paleomagnetic reversal stratigraphy has been determined and chronostratigraphic tie points established by $^{40}Ar/^{39}Ar$ dating of intercalated tuffs. The sequence spans the interval 3.1–2.35 Ma and bears a detailed record of the Gauss/Matuyama paleomagnetic transition. The $^{40}Ar/^{39}Ar$ age for this boundary of 2.589±0.003 Ma can be adjusted to concordance with the Astronomical Polarity Time Scale (APTS) on the basis of an independent calibration to 2.610 Ma, 29 kyr older than the previous APTS age. The diatomites recur at an orbital precessional interval of 23 kyr and are centered on a 400-kyr eccentricity maximum. It is concluded that these diatomite/fluvial cycles reflect a narrow interval of orbitally forced wet/dry climatic conditions that may be expressed regionally across East Africa. The timing of the lacustrine pulses relative to predicted insolation models favors origination of moisture from the northern Africa monsoon, rather than local circulation driven by direct equatorial insolation. This moisture event at 2.7–2.55 Ma, and later East African episodes at 1.9–1.7 and 1.1–0.9 Ma, are approximately coincident with major global climatic and oceanographic events.

Keywords: radiometric dating; astronomical time scale; Gauss/Matuyama boundary; climate change; hominin evolution; East Africa

1. Introduction

Recently, Trauth et al. [1] reviewed the deep-water lake history of the East Africa rift system and identified three humid periods in the past 3 million years, at 2.7 to

* Corresponding author. Tel.: +1 510 644 1295; fax: +1 510 644 9201.
E-mail address: al@bgc.org (A.L. Deino).

0012-821X/$ - see front matter © 2006 Elsevier B.V. All rights reserved.
doi:10.1016/j.epsl.2006.04.009

2.5 Ma, 1.9 to 1.7 and 1.1 to 0.9 Ma, superimposed on a longer-term aridification trend [2]. Interestingly, these episodes of wetter climate correspond to increased aridity in northwest and northeast Africa [3,4], to major global climate transitions [5–10] and major steps in human evolution. However, none of these lacustrine episodes has yet been sufficiently documented to elucidate their precise timing and relationship to changes in the Earth's orbital parameters.

Direct $^{40}Ar/^{39}Ar$ age calibration of orbital climate proxy records in East Africa can address not only related issues in paleoclimatology, but also such diverse topics as time scale calibration and biotic evolution. Detailed paleomagnetic studies in continental sections, when combined with precise correlations to the Astronomical Polarity Time Scale (APTS), can yield estimates of the age and duration of paleomagnetic boundary events that are not subject to the delayed lock-in effects of marine diagenesis.

The present study is an analysis of a fluviolacustrine sequence exposed in the Barsemoi River drainage near Lake Baringo, Central Kenya Rift. This ~200-m-thick sediment package is part of the 5.3–1.6 Ma Chemeron Formation and is one of the examples cited in the compilation of East African lake records of Trauth et al. [1]. The lake history that is recorded at Baringo allows evaluation of events both on a precessional time scale and in the perspective of longer-term climate change. In the fields of paleoecology, paleontology and hominin evolutionary studies, such well-delineated paleoclimate records lay the foundation for testing relationships between climate change and potential responses in faunal communities, and may help elucidate driving forces in hominin evolution.

1.1. Geological setting

The late Cenozoic Chemeron Formation consists of a series of subaerial and lacustrine sediments and siliceous tuffs, discontinuously exposed in the foothills along the eastern flank of the Tugen Hills, a structural horst within the Central Kenyan Rift west of Lake Baringo (Fig. 1). Sedimentary and tuffaceous rocks of the Chemeron Beds, formally designated by McCall et al. [11], were

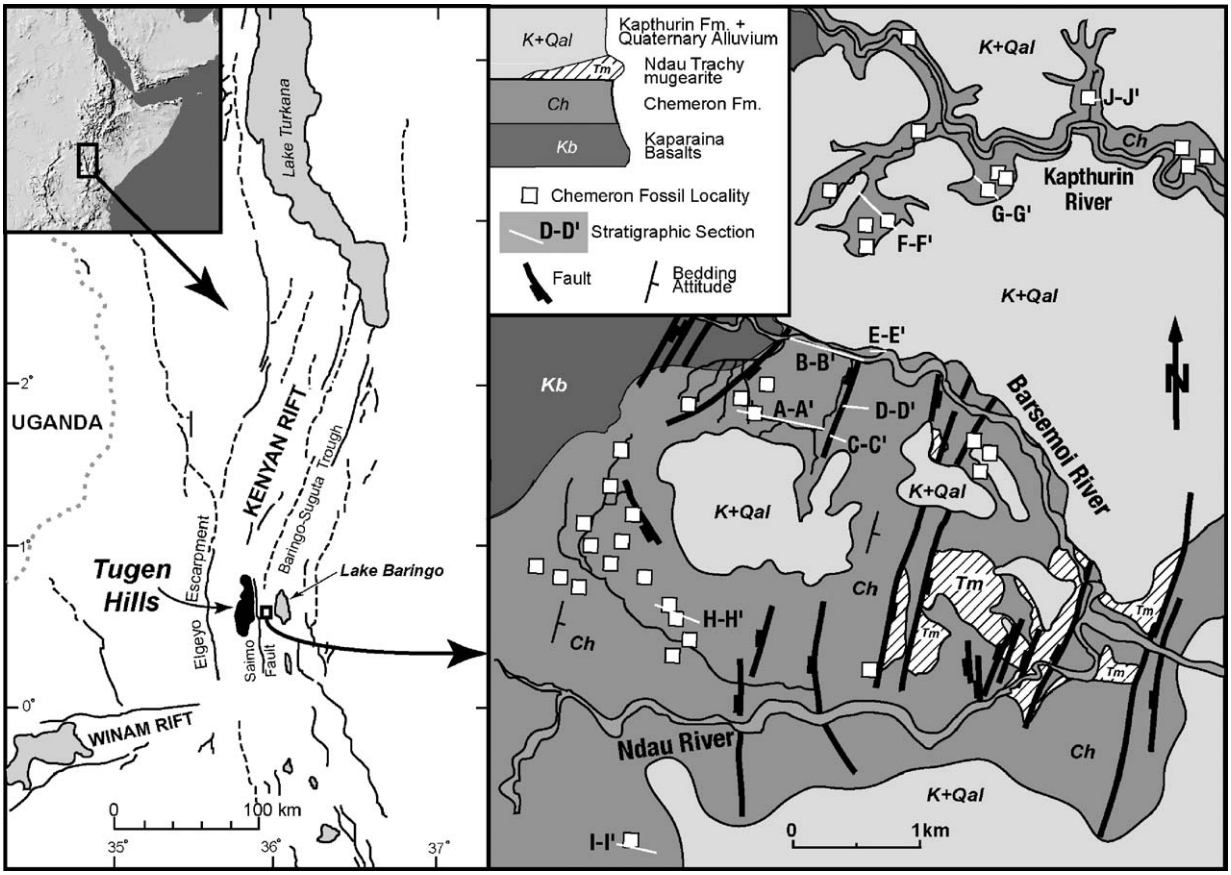

Fig. 1. Location map of the middle Chemeron Formation exposures in the Baringo Basin, central Kenyan Rift Valley.

deposited disconformably on the Kaparaina Basalts and are overlain unconformably by the middle Pleistocene Kapthurin Formation [12–15]. At least two distinct Chemeron depositional basins have been recognized [12,14–16]; the younger Chemeron Basin in the south currently dissected by the modern Chemeron, Ndau, Barsemoi and Kapthurin Rivers, and the Kipcherere Basin 10 km to the north [16]. Isolated exposures of the Chemeron Formation, correlated laterally on the basis of distinctive tuff units [15,17], extend a further 15–20 km to the north of the Kipcherere Basin along the Saimo escarpment.

The Chemeron Formation spans approximately 3.7 Ma, from 5.3 to 1.6 Ma [18]. Published ages for the southern Chemeron Basin range from 3.2 to 1.6 Ma [18,19], with preliminary $^{40}Ar/^{39}Ar$ dating indicating strata as old as 3.5 Ma. The Chemeron Formation here disconformably overlies basaltic lavas and minor intercalated volcaniclastic strata of the 5.7–5.1 Ma Kaparaina Basalt [18,20,21]. The top of the formation occurs slightly above the widespread 1.6 Ma Ndau Trachymugearite flow.

Between 0°30′N and 0°35′N in the Chemeron Basin, the Chemeron Formation occurs within an eastward-dipping structural block frequently cut by ~N–S normal faults. The main Barsemoi River channel cuts through this block primarily in an East–West direction. The Chemeron Formation is here composed mainly of subaerial and lacustrine sediments, mostly mudstone, siltstone and sandstone with intercalations of tuff, diatomite and conglomerate. Within the formation, a distinctive lithologic package characterized by a series of five diatomite units and interbedded fluvial and alluvial fan detritus and tuffs can be traced laterally >5 km N–S along strike. The 3–7-m-thick diatomites consist exclusively of freshwater lacustrine diatom frustules and document significant, intermittent lake systems within the axial portion of the rift. In general, there is a thickening trend in the diatomites eastward, probably as a result of sediment focusing [22], suggesting that deeper portions of the paleolakes were towards the present (and probably paleo-) axis of the rift.

The present study incorporates data from a series of stratigraphic sections across the Chemeron Basin. Attention is focused on two sections exposed in the Barsemoi River drainage spanning 3.1–2.35 Ma (Fig. 2, sections A and E).

1.2. Paleontology

Thirty-five vertebrate fossil localities occur within the formation in the Chemeron Basin. To date, 10 major sites have been tied directly to the portion of the stratigraphic section, which exhibits alternating lacustrine and subaerial conditions. Three fossil sites have yielded hominin fragments, including the oldest specimen of the genus *Homo* at 2.4 Ma [19,23].

1.3. East African climate

Although orbitally induced changes in insolation have been implicated in environmental change in equatorial East Africa, the precise mechanism of how orbital state is translated into climate response remains unclear. Climate in this region is controlled by the seasonal influence of several major air streams and convergence zones, interacting with regional orography, large inland bodies of water and sea-surface temperature fluctuations in the Indian and Atlantic Oceans [24]. As a result, climate patterns are markedly complex and highly variable.

Yearly rainfall cycles in tropical Africa are dominated by the African–Asian monsoonal circulation and seasonal migration of the Intertropical Convergence Zone (ITCZ). Nominally two rainy seasons occur, driven by migration of the ITCZ back and forth across the equator. During the ‘short rains’ in October through December, the ITCZ migrates rapidly southward and the heavy rainfall is of short duration. In contrast, the ‘long rains’ between March and May occur as the ITCZ moves slowly northward, generating heavy rainfall for several weeks. The timing of maximum rainfall lags the position of the overhead sun by 4–6 weeks. Seasonality in rainfall has also been linked to the relative stability of the northeast and southerly trade wind regimes in winter and summer [25] as well as random thermal convection (i.e. isolated thunderstorms not associated with any large-scale disturbances [24]).

The complicated origins and regional diversity of rainfall regimes create difficulties in linking astronomical theory to climate in East Africa. Emerging data indicate that equatorial African climate is affected not simply by insolation changes at low latitudes but also by mid- to upper-latitude insolation changes, which drive systems such as the Asian monsoon and Atlantic sea-surface temperatures. Climate change in equatorial Africa has been linked to high-latitude glacial–interglacial obliquity and eccentricity amplitudes as well as low-latitude precessional insolation changes driving monsoonal circulation intensity. Tropical African rainfall has been specifically linked to orbitally forced insolation changes that affect the strength of the African Monsoon System [26–31]. Formation of sapropels in the eastern Mediterranean Basin caused by increased flux of Nile

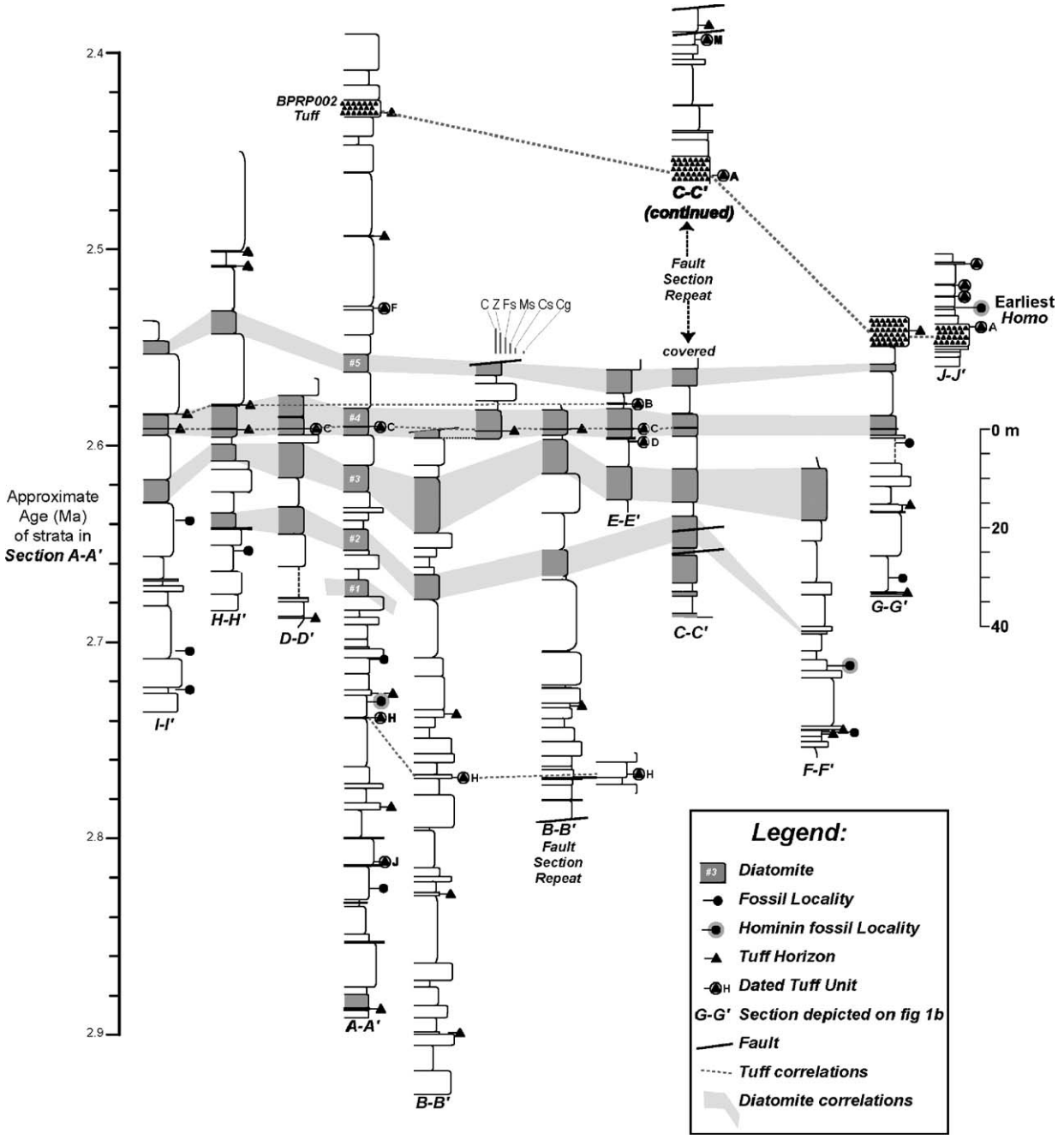

Fig. 2. Stratigraphic sections of the middle Chemeron Formation in the Barsemoi, Kapthurin and Ndau River drainages. Locations of sections are depicted in Fig. 1. Dated tuffs in section J–J′ are documented elsewhere [18,19].

River freshwater [32–34] have also been linked to insolation forcing of East African precipitation. Although an obliquity component has been identified in these studies [4], most implicate precessional forcing. Increased rainfall is associated with strong solar heating in boreal summer, which intensifies the SW African monsoon and the penetration of moist air into equatorial Africa. Thus, precipitation patterns in tropical Africa have typically been linked to calculated orbital insolation curves for June or July at 30°N latitude or greater [35].

Studies of precipitation patterns in the Naivasha Basin over the last 175 ka, however, suggest in part that hydrological changes in East Africa should be

considered in the context of precessional forcing in the spring (March) and fall (September) at the equator which results in greater thermal convection, a strong ITCZ and ultimately greater rainfall [36,37]. Cycling of lake systems as reflected in the Chemeron Formation is therefore considered in the context of precessionally driven changes in insolation at 30°N in June 21 as well as at the equator in March 21 and September 21 (the choice of the 21st of the month derives from options available within *Insola*, a computer program that performs the orbital calculations [38]).

2. Analytical methods

2.1. Paleomagnetism

Magnetostratigraphic studies were undertaken to aid in the refinement of the chronostratigraphy of the Chemeron Formation and calibration of the magnetic polarity time scale by improving age estimates of polarity chrons. Two sections (A and E, Fig. 2), spanning 187 m and 12 m, respectively, were sampled at the Barsemoi locality for paleomagnetism. Characteristic and overprint components of magnetization were determined at the Berkeley Geochronology Center (BGC) using both stepwise thermal and alternating field (AF) demagnetization (details of the paleomagnetic sampling and measurement process are provided in Appendix A).

2.2. $^{40}Ar/^{39}Ar$ dating

The fluviolacustrine section exposed in the Barsemoi River drainage contains at least 10 siliceous tuffaceous horizons distributed subequally throughout the section. Eight of these contain K-feldspar suitable for radioisotopic dating. Analyses were performed at the BGC by the single-crystal, laser-fusion $^{40}Ar/^{39}Ar$ method. Most tuffs were dated in replicate from samples collected in parallel sections. Some samples were further checked for internal reproducibility by replicate analysis of a single mineral separate in more than one irradiation and in more than one location within the irradiation package. Details of the sample preparation, irradiation and outlier detection are provided in Appendix B.

3. Results

3.1. Paleomagnetism

AF-demagnetization results reveal that the majority of samples have a magnetic mineralogy dominated by a soft magnetic mineral. Magnetization versus temperature plots obtained during thermal demagnetization runs indicate Curie temperatures (T_c) of nearly 580 °C. The presence of titanomagnetite, reflecting a stable primary remanence, is most likely the primary carrier of magnetization in these sediments. Some samples, however, show a persistence of remanence above 580 °C, indicating that they contain an additional, higher-T_c mineral such as hematite. This is of some concern as it could reflect a post-depositional remanence. However, similar directions displayed above and below 580 °C reveal that the two phases carry the same direction, suggesting that they were likely acquired simultaneously at, or soon after, deposition.

Although many of the samples yielded well-defined characteristic directions that allowed a straightforward determination of polarity, certain samples presented difficulties due to unstable magnetizations or strong high-stability secondary overprints.

Characteristic remanent directions were calculated using least-squares principal component analysis [39] by fitting lines to at least three successive demagnetization steps. Typical vector analysis plots for samples spanning the transition from the Barsemoi sections are shown in Fig. 3. We assessed the polarity of some samples that did not reach stable endpoints from their great circle demagnetization data by fitting great circles to at least three points and determining whether that great circle path, with increasing levels of demagnetization, trended toward the expected normal or reverse polarity direction. Specimens' circular standard deviations (CSDs, [40]) were typically $<5°$.

For the determination of mean paleomagnetic directions and confidence circles, we used Fisher statistics as modified by McFadden and McElhinny [41] for the inclusion of great-circle data. Site mean CSDs were typically $<12°$. The sampled sections do not offer the opportunity to perform fold or conglomerate tests to assess the stability of remanence. However, mean normal and reverse directions from the Barsemoi A section pass a reversal test [41] indicating that the characteristic remanence directions are not systematically biased by unremoved overprints. For this reason, and because the structurally corrected mean-section direction lies close to the expected GAD field direction, we consider the characteristic directions to be primary, acquired during or shortly after deposition. A summary of the best-fit directions and great circles are shown in Fig. 4.

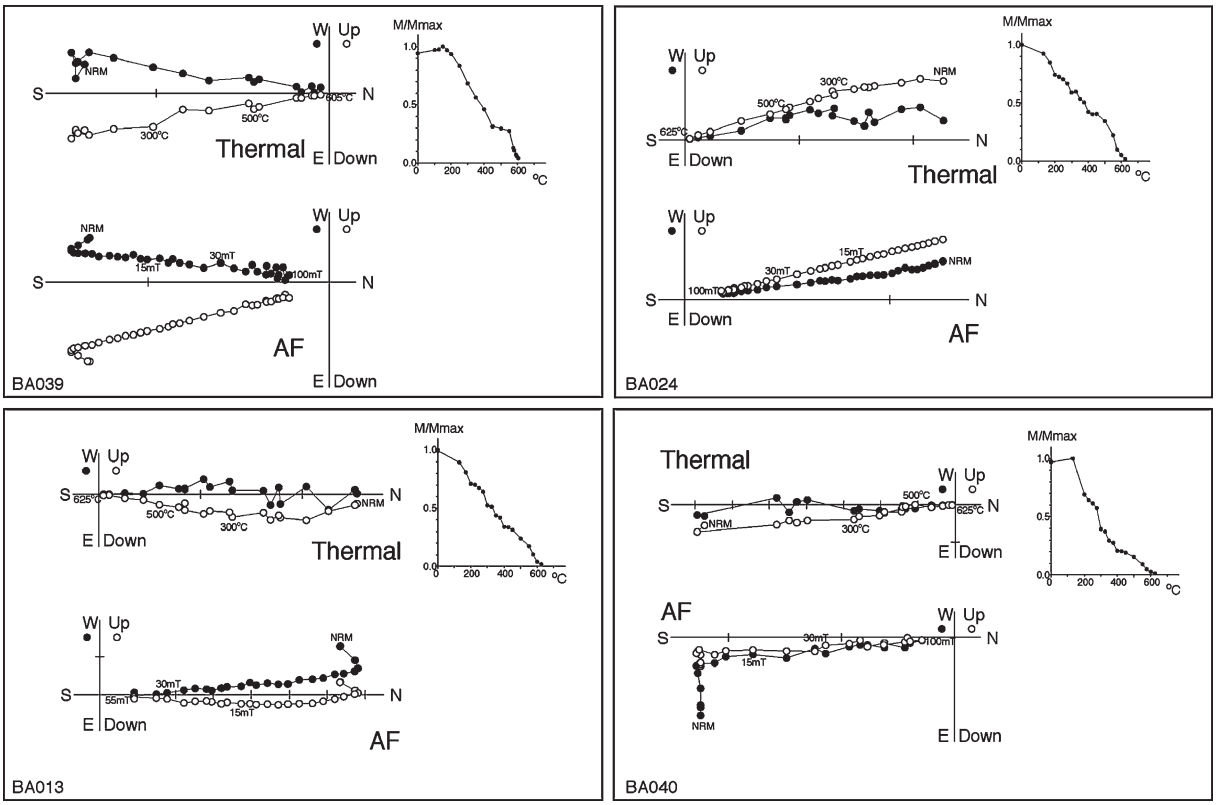

Fig. 3. Typical vector analysis plots for samples spanning the Gauss/Matuyama transition.

These results reveal that the sampled stratigraphy spans a normal-to-reverse (N-R) polarity transition that separates a long normal chron extending to the base of the section from a long reverse chron that continues to the top (Fig. 5). A short normal chron located a few meters above the N-R polarity boundary is identified by a small cluster of samples situated in siltstones at the top of diatomite 5 (for reference, diatomites are numbered from oldest to youngest). These samples yield stable, well-defined directions that show no indication they carry an unusually strong normal overprint. For this reason,

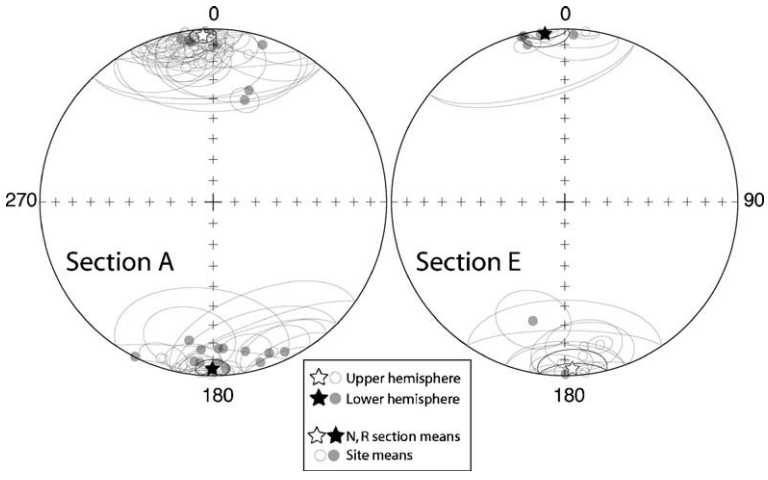

Fig. 4. Stereonet of the structurally corrected best-fit directions and great circles.

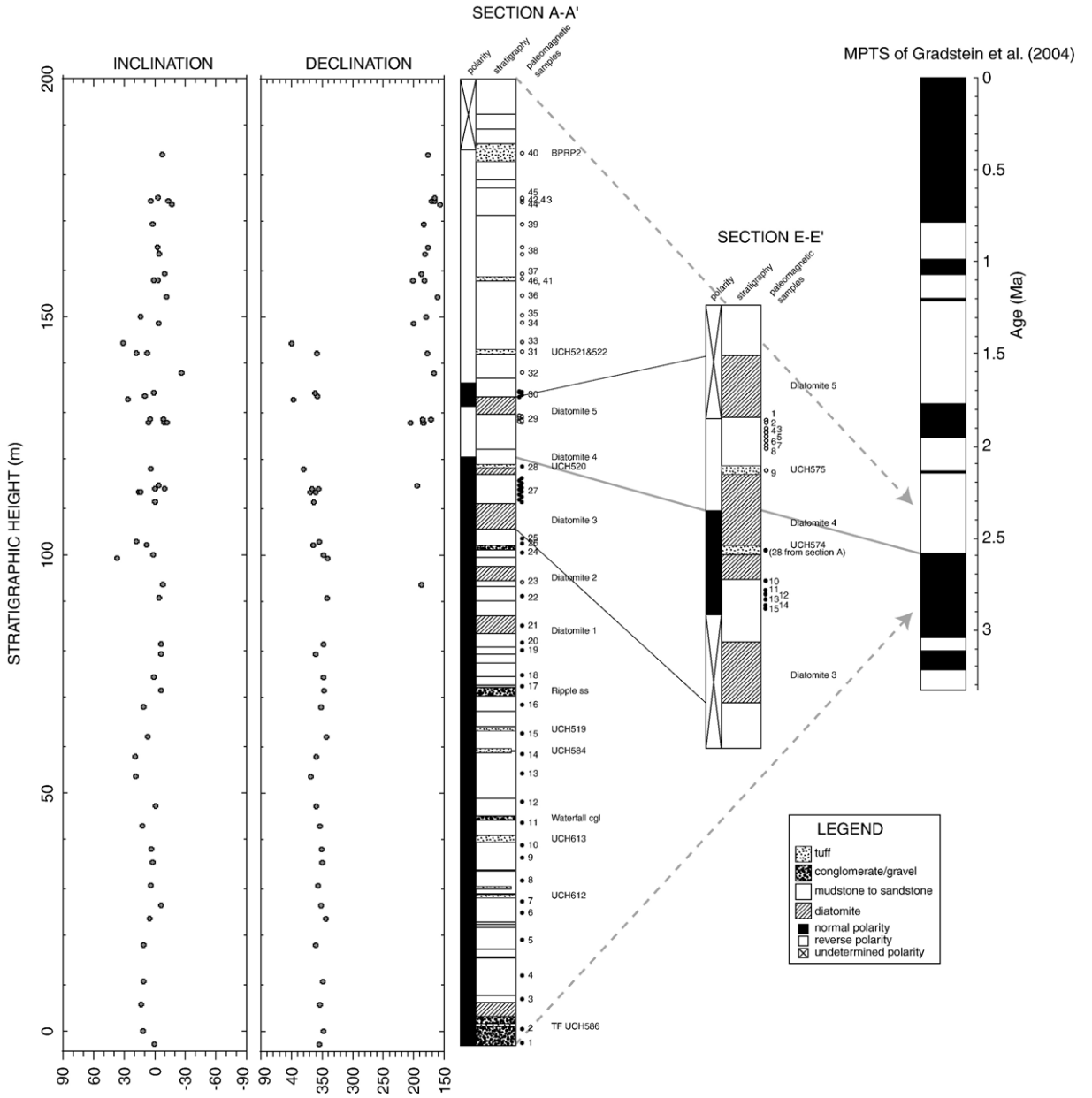

Fig. 5. Magnetostratigraphy. Declination and inclination of sample mean directions (circles) or best-fit specimen directions (triangles) are shown along with the interpreted polarity stratigraphy. Also shown is a correlation of the Barsemoi composite sections magnetostratigraphy with the magnetic polarity time scale [7].

and due to the presence of well-defined reverse directions lying above and below this interval of normally magnetized samples, we interpret this zone as a short polarity chron or excursion following the N-R transition. Given $^{40}Ar/^{39}Ar$ age determinations for this portion of the Chemeron stratigraphy (see below), a correlation of the sections' magnetostratigraphy with the MPTS suggests that the N-R transition corresponds with the Gauss/Matuyama (G/M) polarity reversal. The short polarity chron following the G/M may be a previously unrecognized subchron.

3.2. $^{40}Ar/^{39}Ar$ dating

A summary of the analytical results is given in Table 1, with full analytical details provided online (Table 2 in Appendix C). Age-probability density

spectra illustrate that most samples exhibit unimodal distributions of single-crystal ages from which a primary eruptive age is readily obtained (Fig. 6). Several samples, however, exhibit highly scattered populations with many geologically old ages (BARS97-7 and BARS/94-10, both from Unit H). Four grains from BARS97-7 aggregated from four separate experiments form a discrete, young population that is considered primary (Fig. 6r). A primary component could not be recognized in BARS/94-10 (Table 2 in Appendix C) and this sample is not treated further. Also, sample BARS94-9b (Fig. 6p) exhibited bimodality that could not be readily deconvolved and was excluded from the unit age.

Reduced ages are summarized in Table 1. Weighted-mean ages are calculated hierarchically; aliquots of a given separate are combined to give a weighted-mean sample age and, likewise, the weighted-mean age of a given tuff horizon ('unit') is calculated from individual sample ages. MSWDs with few exceptions indicate the population variability can be entirely accounted for by analytical scatter, at the 95% probability level. Uncertainties are quoted at 1σ and represent the conventional standard error, except in those cases where excess scatter is indicated (MSWD > 1); here, the standard error is magnified by root MSWD.

Robustness of the irradiation procedure is indicated by the reproducibility of aliquots from a single

Table 1
Summary $^{40}Ar/^{39}Ar$ analytical results

Sample	Lab ID#	Irradiation	n/n_0	MSWD	Prob.	Ca/K	Aliquot age±1σ	Sample age±1σ	Unit age±1σ
Unit M:		Pumiceous devitrified tuff 1 m thick							
BARS/94-6	20228	135B	11/12	0.73	0.70	0.012		2.375±0.006	2.375±0.006
Unit A:		Pumice lapillistone 0.5 m thick in the Barsemoi R. area; equivalent to "Lower Tuffs" of Martyn [16]							
BARS/94-1	20232	135B	13/13	2.07	0.02	0.038		2.444±0.009	2.448±0.006
ALD86-1B[a]								2.451±0.008	
Unit F:		White to grey, fine-grained, locally pumiceous and graded, laminated tuff 0.7 m thick							
BARS/94-5p	20234	135B	9/9	1.74	0.08	0.036		2.547±0.007	
BARS97-1a	21053	201A	7/9	0.10	1.00	0.030		2.536±0.007	2.541±0.004
BARS97-1b	21056	201A	10/10	1.35	0.20	0.019		2.540±0.007	
Unit B:		Grey-green, medium to fine-grained, graded ash immediately overlying diatomite							
BARS97-6	21062	201A	13/14	0.28	0.99	0.013	2.589±0.006		
BARS97-6	21405	216A	8/9	1.42	0.19	0.042	2.576±0.010		2.587±0.005
BARS97-6	21417	216B	13/13	2.02	0.02	0.036	2.593±0.010		
Unit C:		Grey to salt and pepper, medium- to coarse-grained, graded, 5 cm thick tuff with small (<1 cm) pumice within diatomite #4							
BARS/94-4	20214	135A	8/14	0.42	0.89	0.024		2.599±0.010	
BARS97-4	21060	201A	20/25	1.26	0.20	0.013	2.595±0.006		2.590±0.003
BARS97-4	21409	216A	11/13	0.48	0.90	0.017	2.584±0.006	2.589±0.004	
BARS97-4	21421	216B	18/20	0.98	0.48	0.011	2.588±0.006		
Unit D:		Reworked tuff/tuffaceous sandstone 5–15 cm thick, 20 cm below diatomite #4							
BARS/97-7	[b]	[c]	4/43	0.39	0.76	0.021		2.596±0.008	2.596±0.008
Unit H:		Pumice-lithic reworked massive to bedded tuff 0.1–1.5 m thick							
BARS/94-3	20226	135B	17/19	1.79	0.03	0.064		2.715±0.011	
BARS/94-7	20230	135B	16/21	1.84	0.02	0.019		2.714±0.010	2.718±0.005
BARS/94-9c	20203	135A	11/11	0.92	0.51	0.020		2.720±0.007	
Rejected:									
BARS/94-9b	20201	135A	7/10	10.55	0.00	0.073		2.81±0.07	
Unit J:		Pumice-crystal-lithic reworked, bioturbated tuff 4–6 cm thick							
BARS/94-2	20222	135B	36/45	3.24	0.00	0.018		2.903±0.012	2.903±0.012

'n/n_0' is the number of individual grain analyses accepted for calculation of the weighted-mean $^{40}Ar^*/^{39}Ar$ sample age, over the total number of analyses performed. 'MSWD' is the mean sum of weighted deviates of the individual ages. Ca/K is calculated from $^{37}Ar/^{39}Ar$ using a multiplier of 1.96. $^{40}Ar^*$ refers to radiogenic argon. 'Aliquot ages' refer to aliquots of a mineral separate irradiated separately. 'Sample ages' refers to weighted-mean ages of separately collected samples of the equivalent tuff. 'Unit ages' refers to weighted-mean ages of individual sample ages of the same tuff. Errors in age are one standard error of the mean and incorporate a 0.2% error in *J* (the neutron fluence parameter). *J* was monitored using sanidine from the Fish Canyon Tuff with a reference age of 28.02 Ma [81]. Samples were irradiated for 7 h in the Cd-shielded CLICIT facility of the Oregon State University TRIGA reactor, in three separate batches. Isotopic interference corrections: $(^{36}Ar/^{37}Ar)_{Ca}=2.72\times10^{-4}\pm1\times10^{-6}$, $(^{39}Ar/^{37}Ar)_{Ca}=7.11\times10^{-4}\pm2.4\times10^{-6}$, $(^{40}Ar/^{39}Ar)_K=7\times10^{-4}\pm3\times10^{-4}=5.543\times10^{-10}$ yr^{-1}.

[a] From equivalent tuff in Kapthurin River drainage, analytical data presented in Deino and Hill [18].

[b] Lab ID numbers 21068, 21070, 21407, 21419.

[c] Irradiations 201A, 216A, 216B.

mineral separate. The analytical separates from BARS97-6 and BARS97-4 were each analyzed three times, encompassing two different irradiations. None of these aliquots can be distinguished statistically from the others of the same mineral separate at the 95% confidence level.

Robustness of the unit ages is indicated by analysis of replicate samples from the same tuff horizon (two samples each for Units A and C, and three samples each for Units F and H). Again, with the exception of BARS94-9b, the replicates are statistically indistinguishable. It can also be noted that K-feldspar from Unit A was first analyzed at BGC by the single-crystal, laser-fusion $^{40}Ar/^{39}Ar$ method in 1987 ([19]; 2.45±0.02 Ma weighted mean of measured ages), again in 1993 ([18]; 2.451±0.008 Ma) and finally in 1995 (this study; 2.444±0.009 Ma). These results are indistinguishable, indicating long- term reproducibility of laboratory determinations to within the stated errors.

3.3. Chronostratigraphy

Stratigraphic section A–A′ (Fig. 2) serves as a reference section for the Chemeron Formation in the Barsemoi River drainage. It is the most complete individual section and extends from the local base of the formation where it is structurally juxtaposed against the Kaparaina Basalts by a normal fault, to within 10 m of the highest stratigraphic level observed in this area (section C–C′, Fig. 2).

Fig. 7a is a plot of unit mean $^{40}Ar/^{39}Ar$ ages against stratigraphic height for A–A′. The oldest calibrated segment, from tuff Unit J at 2.903±0.012 (1σ) to Unit H at 2.718±0.005, encompasses 30 m of sandstone, siltstone, minor conglomerate and tuff. The calculated depositional rate for this interval, 16 cm/kyr, falls within the range of previously determined rates of 11–32 cm/kyr for the Chemeron Formation elsewhere in the Tugen Hills [17,18]. The overlying 123 m between H and A (2.448±0.006 Ma) exhibits a considerably higher overall sedimentation rate of 43 cm/kyr. While nearly linear, the rate shows a slight monotonic decrease upward from 48 to 34 cm/kyr. This sequence is lithologically similar to the underlying section but has a greater proportion of sand and contains toward the middle a sequence of five 3–7-m-thick diatomite beds.

3.4. Diatoms

A preliminary quantitative examination of nearly 500 samples from Chemeron Formation diatomite strata indicates than >90% of all diatoms in each sample, at virtually all levels in each diatomite unit, are euplanktonic species of the genera *Aulacoseira* (e.g., *A. granulata* (Ehr.) Simonsen, *A. agassizi* (Ostenf.) Simonsen) and *Stephanodiscus* (e.g., *S.* cf. *astrea* (Ehr.) Grun., *S.* cf. *hantzschii* Grun., *S.* cf. *subtransylvanicus* Gasse). These assemblages are largely characteristic of East African Pliocene–Holocene diatomaceous deposits [42–47] and contemporary East African large, deep lakes [43,47–49]. The samples display a marked rarity of periphytic plus facultatively planktonic diatoms [44] derived from littoral regions (relative abundance range=0% to 10%, mode=1–2%). Planktonic/(periphytic+facultative planktonic) ratios>100 have been interpreted to indicate deep lakes [1]. Based on this criterion, the Barsemoi lakes would have maximum depths on the order of 150 m. A lack of significant dilution of the diatoms by terrigenous input, an absence of halophilic (saline) diatoms reflecting low lake levels and preservation of intact *Aulacoseira* filaments suggesting anoxic conditions also indicate that the Barsemoi diatomites are the product of large and relatively deep paleolakes [50].

Depositional transitions between diatomites and stratigraphically adjacent fluvial and alluvial fan sediments are characterized by relatively abrupt transgressive and regressive sequences. Diatomites are typically bracketed by 20–30 cm of fine sand and silt horizons, locally containing fish fossils, grading into high-energy terrestrial facies. These sharp transitions indicate relatively rapid (~0.5 kyr) local cycling between lacustrine and fully subaerial conditions.

Detailed sampling (10-cm intervals) across the full exposures of each of the five diatomites reveal significant variation in the relative abundances of *Aulacoseira* [A] and *Stephanodiscus* [S], S/(A+S) (Fig. 7) [50]. This variation has been linked to changes in lake mixing [57,61], which is strongly influenced by climatic variation, with lower S/(A+S) apparently indicating deeper mixing conditions due to cooler, windier conditions [42,46,51]. Interestingly, the proportion of *Stephanodiscus* to *Aulacoseira* varies systematically across the diatomite package. Maximum median proportions (~0.6–0.7) are reached in diatomites #2 and #3, while much lower values (~0.1) are recorded in the first and last diatomites (#1 and #5; Fig. 7g; see [50] for additional details). These proportions suggest that prevailing climatic conditions also varied in a systematic way across the diatomite package, with cooler, windier conditions at the beginning and end contrasting with warmer, milder conditions midway through the diatomite series.

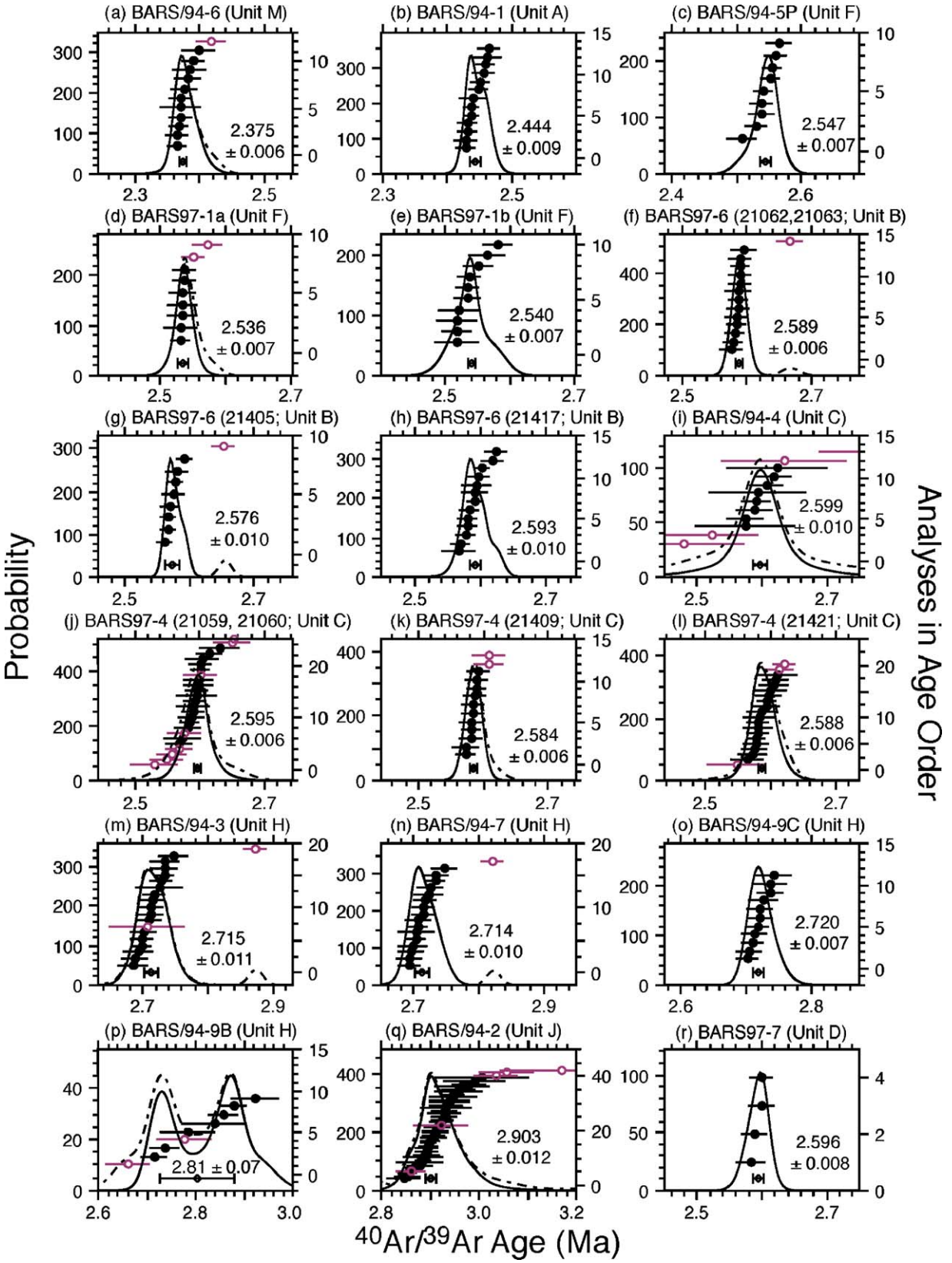
(a) BARS/94-6 (Unit M)
2.375 ± 0.006
(b) BARS/94-1 (Unit A)
2.444 ± 0.009
(c) BARS/94-5P (Unit F)
2.547 ± 0.007
(d) BARS97-1a (Unit F)
2.536 ± 0.007
(e) BARS97-1b (Unit F)
2.540 ± 0.007
(f) BARS97-6 (21062,21063; Unit B)
2.589 ± 0.006
(g) BARS97-6 (21405; Unit B)
2.576 ± 0.010
(h) BARS97-6 (21417; Unit B)
2.593 ± 0.010
(i) BARS/94-4 (Unit C)
2.599 ± 0.010
(j) BARS97-4 (21059, 21060; Unit C)
2.595 ± 0.006
(k) BARS97-4 (21409; Unit C)
2.584 ± 0.006
(l) BARS97-4 (21421; Unit C)
2.588 ± 0.006
(m) BARS/94-3 (Unit H)
2.715 ± 0.011
(n) BARS/94-7 (Unit H)
2.714 ± 0.010
(o) BARS/94-9C (Unit H)
2.720 ± 0.007
(p) BARS/94-9B (Unit H)
2.81 ± 0.07
(q) BARS/94-2 (Unit J)
2.903 ± 0.012
(r) BARS97-7 (Unit D)
2.596 ± 0.008
Probability
Analyses in Age Order
40Ar/39Ar Age (Ma)

In summary, the Barsemoi diatomites are apparently the products of paleolakes that were moderately deep (minimally 30–40 m and plausibly >150 m), areally significant (several hundreds of square kilometers) and stable (ca. 5–10 ka) features of the Pliocene landscape. Proportions of key diatom species suggest that climatic conditions varied systematically between diatomites.

4. Discussion

4.1. Calibration of the Gauss/Matuyama boundary

The G/M magnetic polarity transition was identified within the upper two-thirds of diatomite 4, bracketed between a tuff with normal polarity (Unit C), located within the diatomite, and a tuff (Unit B) immediately overlying the diatomite with reversed polarity. The $^{40}Ar/^{39}Ar$ ages for Units C and B are 2.590±0.003 Ma and 2.587±0.005 Ma, respectively, and the boundary age is taken as the weighted mean, 2.589±0.003 Ma. Normalization of this $^{40}Ar/^{39}Ar$ age to orbital time scales using the intercalibration discussed in detail in Section 4.6 below yields 2.610 Ma for the G/M boundary.

This age is virtually identical to a recent assignment of 2.608 Ma for the boundary based on multiple open-ocean marine cores orbitally tuned using benthic foraminefera $\delta^{18}O$ records [52], but is 29 kyr older than the Mediterranean APTS-based estimate [7]. This latter discrepancy is beyond analytical error and is consistent with diagenetic lock-in delays influencing the acquisition of magnetism in the relevant Mediterranean section in Singa (Calabria, southern Italy).

4.2. Periodicity of climate change

Interpolated ages for the upper and lower contacts of diatomite horizons are shown in Table 2, calculated assuming linear sedimentation rates between bracketing dated tuffs. Diatomite deposition spans ~100 kyr from 2.665 Ma to 2.562 Ma. The median interval between the onset of the diatomite sedimentation cycles is 23.2 kyr (range 22–27 kyr) and between their termination is 23.4 kyr (range 22–28 kyr). Deep lacustrine conditions (diatomites) occupied a median 8 kyr of the full cycle (7–12 kyr), whereas relatively dry conditions (all other sediments) persisted about twice as long (15 kyr, range 12–16 kyr).

4.3. Precessional climate forcing

Perhaps the most compelling evidence for orbital control of the rhythmic diatomite/subaerial sedimentation sequence in the Barsemoi centered at ~2.6 Ma is the match of predicted precessional periodicity to chronostratigraphy. Employing a simple linear sedimentation model between radiometrically calibrated tie points yields a median interval between the onset of lacustrine cycles of 23.2 kyr, compared to the 22.5-kyr periodicity of the insolation curve (30°N latitude, June 21) for this time range calculated from the orbital solutions [38] (Fig. 7b). This remarkably good match, encompassing five successive wet/dry cycles, suggests that the rhythmic Barsemoi lithostratigraphy records precessionally forced climate change in this part of East Africa, in a uniform tectonic environment that persisted for at least 270 kyr between Units A and H.

Internal variations described above in the relative abundances of *Aulacoseira* and *Stephanodiscus* within the diatomites also supports orbital forcing of the moisture accumulation. Spectral analysis of Holocene diatom profiles from Lake Victoria, demonstrating similar long-term periodicities to those observed at Baringo, have been linked to global-scale climatic oscillations [42].

Collectively, the diatomite chronostratigraphy and internal species variations demonstrate that the cycling of lake facies is controlled principally by changes in the precipitation and evaporation balance in the Baringo Basin and by hydrographical mixing dynamics in its paleolakes during the Plio-Pleistocene, rather than in response to tectonic uplift or accommodation associated with rifting.

4.4. Rate of diatomite deposition

The chronostratigraphy presented above assumes that deposition proceeded at a uniform rate between radiometric tie points. This assumption is perhaps least valid for diatomites compared to the subaerial intervals. Geological examples from elsewhere in East Africa offer

Fig. 6. Age-probability plots of $^{40}Ar/^{39}Ar$ dating results. Individual analyses with 1σ analytical uncertainty are shown by circles with horizontal error bars, ordered vertically by increasing age. Open symbols represent excluded analyses. The weighted mean age and 1σ analytical uncertainty (including error in *J*, the neutron fluence parameter) are shown numerically and by the diamond symbol with error bars. Solid curves represent the age-probability density spectrum for included analyses only; the dashed curve includes all analyses. All graphs are plotted using horizontal axis scale of 0.3 Ma range, with the exception of (g) and (h), which encompass 0.4 Ma. Older analyses may be off the scale of the individual graphs (see Table 2 for all analyses).

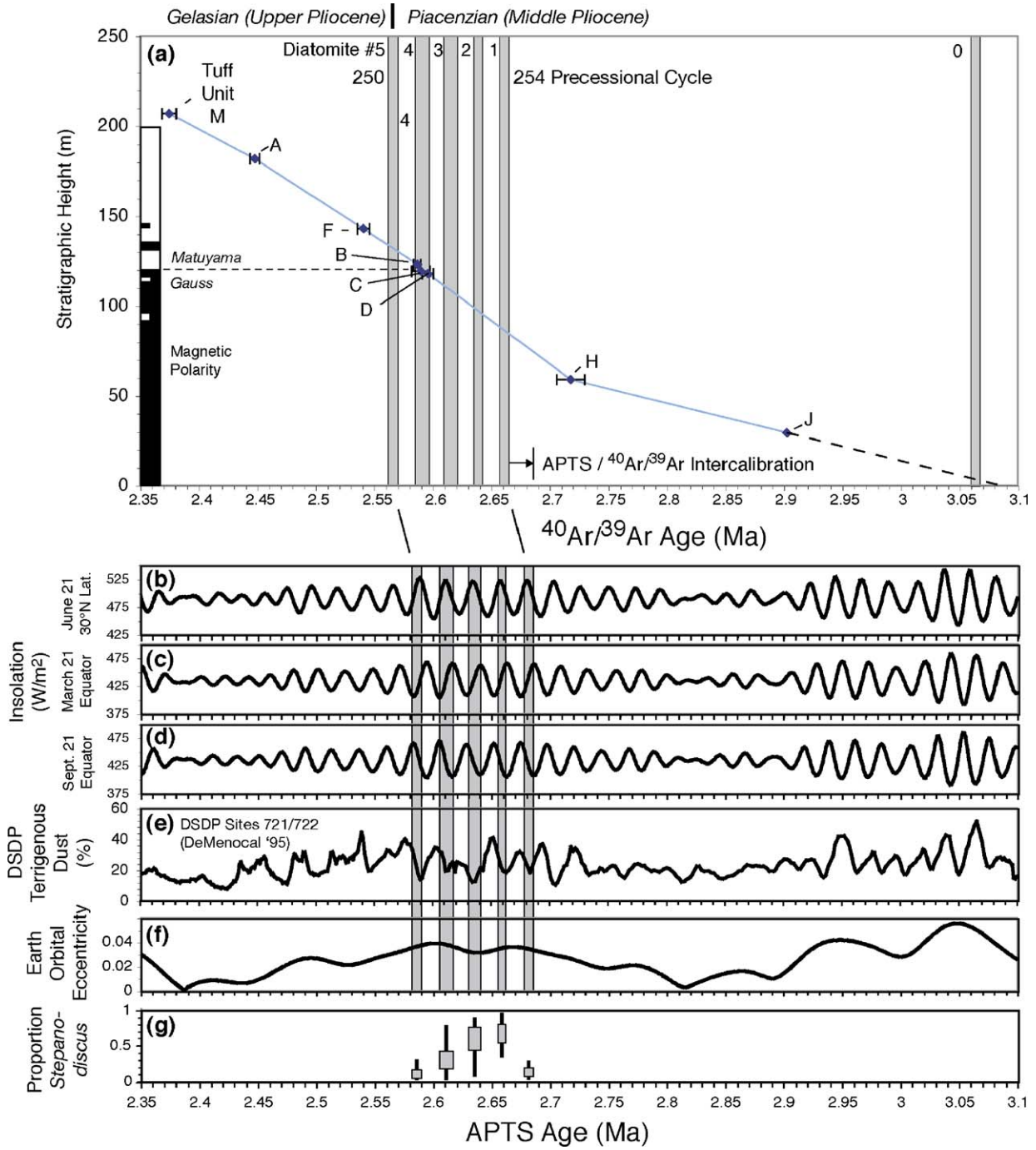

Fig. 7. (a) $^{40}Ar/^{39}Ar$ age vs. stratigraphic height for section A–A′. Unit-mean $^{40}Ar/^{39}Ar$ ages are plotted with 1σ standard error. Magnetostratigraphy is shown on the left. The dashed line from Unit J to the base of the section is a projection of the sedimentation rate from H to J. Diatomites are numbered from oldest (0) to youngest (5) based on superposition in the Barsemoi sections and are identified with the corresponding precessional cycle number counted from the present. The 'APTS/$^{40}Ar/^{39}Ar$ calibration' refers to the adjustment necessary to bring the measured $^{40}Ar/^{39}Ar$ ages into agreement with the APTS, based on an independent calibration [56,57]. Diatomite intervals portrayed in (b)–(e) have been adjusted on this basis to the APTS time scale. (b) Calculated insolation [38] for June 21 at 30°N latitude plotted against APTS age. (c) Calculated insolation for March 21 at the equator. (d) Calculated insolation for September 21 at the equator. (e) Eolian dust record for DSDP Sites 721/722 in the Arabian Sea [4]. (f) Earth orbital eccentricity. (g) Box-and-whiskers plot of *Stephanodiscus* to *Aulacoseira* diatom proportions, showing the median, the interquartile range (50% of the data about the median) and the full range of the data.

Table 2
Diatomites

Diatomite #	Diatomite level	Stratigraphic height (mab)	Interpolated $^{40}Ar/^{39}Ar$ age (Ma)	APTS-adjusted age (Ma)	Thickness (m)	Duration (onset)	Length dry interval (kyr)	Length wet interval (kyr)	Insol. 0°, March 21		Insol. 30°, June 21	
									Age of max. insol. (Ma)	Offset to diatomite (kyr)	Age of max. insol. (Ma)	Offset to diatomite (kyr)
5	Top	133.5	2.562	2.583								
	Middle	131.7	2.566	2.586	3.5				2.595	9	2.589	3
	Bottom	129.9	2.570	2.590				8				
						27	15					
4	Top	123.2	2.585	2.606								
	Middle	120.5	2.591	2.612	5.5				2.617	5	2.611	−1
	Bottom	117.7	2.597	2.617				12				
						24	12					
3	Top	111.8	2.609	2.630								
	Middle	109.1	2.614	2.635	5.5				2.641	6	2.635	0
	Bottom	106.3	2.620	2.641				11				
						23	16					
2	Top	98.4	2.636	2.658								
	Middle	96.9	2.640	2.661	3.1				2.664	3	2.658	−3
	Bottom	95.3	2.643	2.664				7				
						22	15					
1	Top	87.8	2.658	2.680								
	Middle	86.2	2.662	2.683	3.1				2.687	4	2.680	−3
	Bottom	84.6	2.665	2.686				7				
Average:					4.2	23.8	14	9		5.4		−0.8
Median:					3.5	23.2	15	8		5.4		−0.6

'mab' is meters above base of section A–A′.
'Offset to diatomite' is the difference between the age of the insolation peak and the APTS-corrected diatomite midpoint age.

little basis for a priori assignment of Barsemoi diatomite sedimentation rates; these vary over almost two orders of magnitude, and in environments that may have been most similar to those of the Pliocene Baringo basin range from 10 cm/kyr at Gadeb, Ethiopia [44] to as much as 100 cm/kyr at Olorgesailie, Kenya [53]. A direct measurement of diatomite sedimentation rate derived from the $^{40}Ar/^{39}Ar$ ages bracketing and within the 5-m-thick diatomite #4 yielded a rather poorly constrained sedimentation rate of 230 cm/kyr (95% confidence interval 30–1200 cm/kyr, utilizing Bayesian interval estimation [54]). In light of the uncertainties in determining a representative diatomite sedimentation rate, stratigraphic rate calculations are presented here assuming a simple linear sedimentation model. However, if the sedimentation rate for diatomite is somewhat faster than the subaerial section, shorter lake durations, more rapid lacustrine/subaerial transitions and shorter periodicity to the lacustrine cycles would result.

4.5. Modulation by orbital eccentricity

Insolation amplitude variations during this interval are dominated by precession but modulated by orbital eccentricity. The peaks of two 400-kyr eccentricity cycles can be seen in Fig. 7f at ~3.1–2.9 Ma and ~2.7–2.55 Ma. This latter period encompasses the sequence of lacustrine cycles recorded in the Barsemoi River section (2.67–2.56 Ma). Lacustrine sediments are absent from the remainder of the section corresponding to reduced eccentricity, hence precessional amplitude. Although subaerial sedimentary characteristics and depositional rate are similar throughout A–H, lakes are absent from this youngest part of the section.

Below Unit H, fluvial sedimentation increases, accumulation rates slow and lacustrine sediments are nearly absent. This may reflect either a contrasting tectonic environment compared to A–H, or drier climatic conditions accompanying the eccentricity minimum at ~2.9–2.8 Ma.

Eccentricity increases again from ~3.1 to 2.9 Ma, resulting in precessional insolation swings even greater in amplitude than those of the 2.7–2.55-Ma interval. Although there are no datable tephra below Unit J at 2.903±0.012 Ma, extrapolation of the H–J sedimentation rate suggests that the lower 30 m of section A–A′ coincides with this interval of maximal insolation amplitude. A single 2.5-m diatomite occurs at a

projected age of ~3.1 Ma, just before the section is truncated by a major fault (Fig. 2). This lacustrine event may be a response to precessional climate control under environmental conditions similar to those which generated the diatomites higher in the section. It is unclear why only a single lacustrine event was recorded at a time of such extreme insolation maxima, but this may reflect regional, even global, phenomena (see below).

4.6. Correlation to the astronomical time scale and evaluation of climate models

The most likely interpretation of the 23-kyr periodicity of wet/dry cycles in the Barsemoi River drainage is that it reflects the influence of the Earth's precession on lake development in this part of East Africa. However, a precise correlation of diatomites to calculated orbital cyclicity remains to be established.

The most direct approach is to compare the $^{40}Ar/^{39}Ar$ calibrated diatomite ages to orbitally calculated insolation maxima. Although the weighted-mean unit ages have "internal" analytical errors from 0.1% to 0.4%, the absolute or true age is subject to much greater systematic errors, arising from uncertainties in the rates of radioactive decay, isotopic abundances and absolute calibration of the neutron fluence standard. This 'external' error is on the order of 1–2% [55], or 25–50 ka, equal to one or two precessional cycles. This systematic error hampers efforts to directly compare the radiometric ages measured at Baringo to the theoretically calculated astronomical solutions to the paleoinsolation curves.

One way to compensate for this problem is to use an independent intercalibration of the astronomical time scale with carefully determined $^{40}Ar/^{39}Ar$ ages. Kuiper [56] and Kuiper et al. [57] have compared high-precision $^{40}Ar/^{39}Ar$ ages to the APTS in orbitally tuned Mediterranean sequences in Morocco and Crete, employing the same dating standard as this study, sanidine from the Fish Canyon Tuff of Colorado. They propose a revised age for the standard that would force adjustment of $^{40}Ar/^{39}Ar$ ages to agree with the APTS; this is effectively a 0.8% increase in $^{40}Ar/^{39}Ar$ ages for the Neogene. BGC is collaborating with the Amsterdam/Utrecht intercalibration effort and we have confirmed the observed offset to ±0.1% bias.

The Barsemoi $^{40}Ar/^{39}Ar$ ages can thus be adjusted by this intercalibration relationship to force agreement with the APTS and compared directly to several possible orbital insolation curves (Fig. 7b–d). Three paleointensity curves are considered, due to the possibly contrasting moisture influences acting on this part of the African continent: March 21 at 0° latitude representing direct equatorial insolation (the middle of the 'long rains' when rainfall is greatest in the modern equatorial Rift Valley), September 21 (the 'short rains') and June 21 at 30°N latitude (boreal summer) reflecting the influence of the northern monsoon system. The adjusted diatomite ages demonstrate generally consistent phase relationships with the three calculated insolation curves; the diatomites neatly coincide with the insolation peaks of the June 21/30°N curve, but lie midway along the falling edge of the March 21/0° curve and on the rising edge of the September 21/0° curve. Thus the match of insolation maxima to climate response in terms of moisture accumulation is better for the June 21/30°N curve than either equatorial model, suggesting that the northern monsoon system exerts dominant climate control over this part of East Africa at ~2.6 Ma. This is an interesting contrast to modern conditions, where direct equatorial insolation during the long and short rains appears to dominate the hydrological balance of the nearby Naivasha Basin [36,37].

4.7. Synchroneity with regional and global climate change

The Barsemoi lakes did not arise in paleoclimatic isolation, but instead are part of a broader picture of lake development across East Africa at this time. Trauth et al. [1] review the history of lake development in the region during the last 3 Ma, and identify three major wet periods from 2.7 to 2.5, 1.9 to 1.7 and 1.1 to 0.9 Ma. One of the two examples used to support increased moisture levels at 2.6 Ma is the Baringo diatomite sequence discussed herein; the other is on the eastern shoulder of the Ethiopian Rift at Gadeb, Ethiopia (2.7–2.4 Ma) [58]. These regional humid periods correspond to eccentricity maxima and develop at least partially in response to orbital forcing.

However, there are also intervals where eccentricity maxima, hence maxima in precessional insolation amplitude, are not accompanied by humid conditions. The Barsemoi sections provide an example; diatomites are nearly absent from the eccentricity maximum at 3.1–2.9 that preceded the 2.7–2.55-Ma event.

The specific response that resulted in the wet periods of the last 3 million years may reflect increased sensitivity or intensification of the African monsoonal system as a response to major global climate change. The wet period from 2.7 to 2.5 Ma corresponds to the onset and intensification of Northern Hemisphere

glaciation ("ONHG"), one of the critical climate thresholds of the Cenozoic [5,6], 1.9–1.7 Ma to a significant shift in the Walker Circulation (east–west atmospheric circulation pattern over the Pacific) [8] and 1.0–0.8 Ma to the initiation of the mid-Pleistocene Revolution (shift from 41 to ~100 kyr glacial–interglacial cycles) [9,10]. The East African lacustrine episodes also coincide with or just precede major oceanic events including spikes in bipolar ice-rafted debris flux, eustatic highstands and suppressed North Atlantic Deep Water formation [59]. West and East African eolian records indicate a shift from 23 to 19 kyr precession to 41 kyr variations [4] near 2.8 Ma, suggesting that African climatic patterns became more dependent on the rhythm of high-latitude climate change once northern hemisphere ice sheets attained sufficient size. Formation of the Barsemoi lakes during this transition may reflect interactions between global climate boundary conditions and shifts in the African monsoon intensity related to orbital forcing.

The Barsemoi lake cycles may be compared to the orbitally tuned climate proxy record obtained from DSDP Site 721/722 in the Arabian Sea. Approximately 1000 km northeast of Kenya, this site contains a detailed record of eolian dust influx interpreted as corresponding to alternating wetter and drier conditions in subtropical Africa [4,27]. This comparison bears on the debate concerning global vs. local forcing of East Africa climate [1,4,27,36,60,61]. Because of the unique tectonic evolution of the East African Rift System (EARS) and resulting changes in orography and drainage patterns, Indian Ocean marine sediment records do not necessarily reflect coeval environmental change in East Africa. For example, Trauth et al. [1] observed anti-correlation of the eolian dust record off East and West Africa with lacustrine conditions in East Africa on the 100-kyr time scale. However, the new Baringo data indicate that, at shorter precessional intervals, cyclical dips in the dust concentration record corresponding to wetter conditions in subtropical Africa are nearly synchronous with the Baringo diatomite package (Fig. 7e). Correlated climate responses between subtropical Africa and the Central Kenya Rift is permissive evidence that an integrated regional climate mechanism is at work.

Synchroneity of the Barsemoi lakes and minima in the Arabian Sea terrigenous dust abundance implies that the antiphase relationship is also correlated: maxima in the DSDP dust record at times of deep precessional insolation minima may also indicate extremely dry conditions in this part of East Africa (offset by about 11.5 kyr from the lacustrine cycles). There is as yet no direct evidence of extreme aridity in the Barsemoi sequence at these times, though isotopic studies have been initiated to test this hypothesis. High-resolution analyses of intra- and inter-tooth isotopic variability in herbivore lineages will potentially provide a proxy for seasonality and evaporative/precipitation patterns, and ultimately a framework for interpreting specific terrestrial ecological response to these cycles.

It is noteworthy that a prominent dip in the DSDP dust concentration record at 2.71 Ma immediately preceding the diatomite series is not matched by lacustrine sedimentation in the Barsemoi River sections. One explanation might be an error of one precessional cycle in the astronomical tuning of this portion of Sites 721/722. However, this is related to the circumstance noted above, where a high amplitude insolation peak at 2.7 Ma was unaccompanied by a lake bed. There are many possible reasons why a diatomite might not be recorded in the Barsemoi sections at this apparently favorable time, ranging from simple geological causes (e.g., concurrent structural tilting of the basin; subsequent erosion of the lake sediments), to poorly understood climate threshold barriers and forcing factors (e.g., contribution from ONHG, maximum seasonality vs. simple insolation). Indeed, a lake may have formed, but in a more axial part of the basin than has yet been observed. Survival of an early, relatively small lake through the subsequent dry cycle may have set the stage for the even deeper lakes that ultimately inundated the Barsemoi River area. However, internal evidence suggests another possible explanation: systematic variations in *Stephanodiscus* to *Aulacosera* diatom ratios across the diatomite package define the limits of a coherent ~100-kyr climatic cycle (Fig. 7) and the elevated-insolation peak at 2.7 is simply outside the bounds of this phenomenon.

Inter-diatomite variation in *Stephanodiscus* to *Aulacosera* diatom ratios provides additional perspectives on the nature of climatic variation spanning the Barsemoi paleolake interval. Insolation peaks across this time interval are near equal in intensity and it is difficult to reconcile insolation factors with the observed systematic trends in inferred climate/prevailing wind conditions. While the trend in diatom proportions in the Barsemoi diatomites may result from cumulative effects as the paleolakes retreat and expand throughout this interval, alternatively, it may hint at the influence of additional external climate forcing factors or internal feedback mechanisms. This systematic variation across the interval of diatomite deposition remains one of the intriguing conundrums of the Barsemoi record. A very similar pattern in the abundance of *Stephanodiscus* was

observed in the contemporaneous diatomite record at Gadeb, suggesting that it is a regional phenomenon [58].

4.8. Relationship to hominin evolution and faunal change

The Piacenzian to Gelasian (3.6–1.8 Ma) represents a critical period in hominin evolution. This interval features the earliest evidence for tool use [62] and butchering sites [63], significant increases in brain size [64], development of modern human body proportions [65], the origin of genus *Homo* [18,19,23] and the dispersal of hominins from Africa [66]. In addition, a series of speciation events suggest an adaptive radiation in the hominin lineage between 3 and 2 Ma [67–71]. Reconstructing the ecological context of these morphological and behavioral innovations is critical for interpreting their adaptive significance and much research has focused on establishing links between hominin evolutionary events, and global, regional and local environmental perturbations [4,72,73].

While long-term climate trends no doubt influenced human evolution, it has become evident that climatic control of mammalian evolution is more complex than supposed and that East Africa is characterized by almost continuous flux and oscillation of climatic patterns driven primarily by astronomical forcing [4,74]. The complex interaction of orbitally induced changes in insolation and earth-intrinsic feedback mechanisms results in extreme, inconsistent environmental variability which have been linked to behavioral and morphological mechanisms that enhance adaptive variability in hominin evolution. Although Plio-Pleistocene evidence of short-term climatic change in the East African Rift has been documented at a number of early hominin sites, including Olduvai [75], Olorgesailie [76], Hadar [77] and Turkana [78], it has been difficult to unequivocally link these perturbations to astronomically mediated insolation patterns. The Baringo data provide the only empirical evidence for significant local environmental shifts that can directly be correlated with insolation patterns and can provide key insights into the nature of evolutionary change in the context of orbitally forced environmental flux.

The sharpest climatic shifts occur at the wet-to-dry (desiccation) and dry-to-wet (humidification) transitions, which are less than about 1000 yr in duration and occur alternately every ~11.5 kyr. Desiccation presumably exerts different selective pressures than humidification; evolutionary change induced in one kind of transition has multiple opportunities to be reinforced every ~23 kyr in corresponding periods of later precessional cycles. This 'opportunity' for evolutionary change is centered at the peak of an eccentricity maximum and may last only ~100 kyr, based on the moisture record afforded by the Barsemoi sequence. Ongoing research in the Baringo Basin is focused on examining and correlating patterns of evolutionary and climatic change that may be linked to precessional cycling.

5. Conclusion

Piacenzian–Gelasian fluviolacustrine sediments of the fossiliferous Chemeron Formation are exposed in a series of correlated sections on the eastern flank of the Tugen Hills within the axial portion of the Central Kenya Rift. This sequence contains a 2.66–2.54-Ma package of five successive cycles of 3–7 m thick, pure diatomites alternating with subaerial sediments. The almost exclusive presence of the planktonic genera *Aulacoseira* and *Stephanodiscus* in the diatomites, and the virtual absence of detrital grains, suggest deep, areally extensive lake systems. The diatomite beds exhibit a median spacing of ~23 kyr, equivalent to the periodicity of insolation maxima of 22.5 kyr calculated from orbital parameters for this time interval [38]. This agreement is strong evidence that wet/dry conditions recorded here are orbitally forced and not related to tectonic perturbations of the basin. Lacustrine conditions occupy less than a third of each precessional cycle ($\leq$8 kyr). Transgression and regression of the lake systems were rapid; local transitions between lacustrine and fully terrestrial conditions may have taken less than 0.5 kyr.

Comparison of the APTS-adjusted ages of Barsemoi diatomites with several equatorial and northern hemisphere paleointensity curves suggests that summer, 30°N latitude provides the best match of insolation maxima to observed wet intervals. Evidently, the northern latitude summer monsoon had a greater influence on the hydrologic budget of equatorial East Africa at this time than direct insolation.

The G/M paleomagnetic transition was identified within the upper part of the second youngest diatomite, in an interval tightly bracketed by high-precision $^{40}Ar/^{39}Ar$ determinations. The radiometric age of the boundary is 2.589±0.003 Ma with a maximum duration of the transition of 1.5 kyr (+12 and −1.5 kyr at 95% confidence level). Corrected by +0.8% to APTS ages [56,57], the boundary is 2.610 Ma, 29 kyr older than the Mediterranean APTS-based estimate [34].

Lacustrine conditions in Baringo at the Piacenzian/Gelasian boundary correspond to an interval when eccentricity, hence precessional insolation variation, was at a maximum. These deep-lake conditions are part of a series of three regional wet periods in East African

in the last 3 Ma [1]. In a global perspective, the Baringo diatomite package occurs at about the same time as major climatic and oceanographic milestones, such as the onset of Northern Hemisphere glaciation, eustatic highstands and bipolar ice-rafted debris flux [59].

The profound wet/dry oscillations from 2.7 to 2.5 Ma may have had particular influence on hominin evolution. This period, and shortly thereafter, is noted for several hominin evolutionary milestones including the earliest record of stone tool manufacture (~2.6–2.5 Ma [62]), the nearby appearance of the genus *Homo* (2.4 Ma [18,19]), earliest *P. boisei* (2.4 Ma [79]) and the only known specimens of *Australopithecus garhi* (~2.5 Ma [63]).

Acknowledgments

We would like to thank Peter Kiptalam for assistance in paleomagnetic sampling and Boniface Kimeu for assisting with various field logistics. This work was supported by NSF grants 9405347 and 9903078 to AD, Emory University URC grant to JK and grants to AH from Clayton Stephenson, and from the Schwartz Family Foundation. Martin Trauth, Mark Maslin, Lucas Lourens and Gary Scott provided valuable discussion, and the manuscript was greatly improved based on Martin's review. This work forms part of the research of the Baringo Paleontological Research Project, directed by AH, based at Yale University and undertaken in collaboration with the National Museums of Kenya (NMK). Authorization for research and excavation comes in the form of permits to AH (OP/13/001/C 1391) from the Government of the Republic of Kenya.

Appendix A. Paleomagnetic sampling and measurement

Most of the Barsemoi sediments consisted of poorly consolidated material that was difficult to drill. Sampling was typically restricted to fine-grained material consisting of siltstones and mudstones, and occasionally ashes. However, at a few horizons where this was not possible, courser materials, up to fine-grained sandstones, were taken. The sampling sites were first excavated using shovels and picks, to remove weathered material. Magnetically oriented samples were then taken in one of three ways: with a portable, battery-powered electric saw following a method similar to that described by Ellwood et al. [80]; by hand-carving 1-cm^3 cubes from the outcrop using non-magnetic Cu–Be tools; or by extracting fist-sized hand samples that were later subsampled in the laboratory, using a bandsaw, to yield 1-cm^3 cubic specimens for rock- and paleomagnetic measurements.

Samples were grouped into sites that were distributed at roughly 1–3-m intervals. Site positions, however, depended on the availability of fine-grained material. Typically, three or more samples were taken at each site and roughly from the same stratigraphic horizon, though at a few sites, additional samples were taken and were distributed vertically through the section for higher resolution magnetostratigraphy. Where samples lay at the same stratigraphic height, their directions were averaged.

Paleomagnetic measurements were performed in shielded rooms at the BGC's paleomagnetism laboratory using 2G Enterprises cryogenic magnetometers. We applied both stepwise thermal and alternating field (AF) demagnetization (generally consisting of more than 15 steps) to samples to determine characteristic and overprint components of magnetization. AF demagnetizations were performed with a 2G two-axis AF demagnetizer and thermal demagnetizations were carried out in air in an ASC shielded furnace.

Appendix B. $^{40}Ar/^{39}Ar$ technique

All $^{40}Ar/^{39}Ar$ analytical work was performed at the BGC. Samples were gently disaggregated using a ceramic mortar and pestle, and sieved to extract the 0.35–1.2-mm size fraction. Wherever possible, extraction was performed on pumice in preference to bulk tuff. K-feldspar phenocrysts were concentrated using magnetic and heavy-liquid separation techniques, where necessary. The mineral separates were treated with dilute HCl, HF and distilled water in an ultrasonic bath to remove adhered matrix, and hand-selected to obtain pristine, inclusion-free feldspars.

The K-feldspar crystal concentrates were irradiated in three 7-h batches in the Cd-lined, in-core CLICIT facility of the Oregon State University TRIGA reactor. Sanidine from the Fish Canyon Tuff of Colorado was used as a mineral standard, with a reference age of 28.02 Ma [81]. Standards and unknowns were placed in 2-mm diameter by 2-mm deep wells in a circular configuration [82]. Standards were spaced either every other hole or every two holes. Planar regressions were fit to the standard data and the neutron fluence parameter, *J*, interpolated for the unknowns. Residuals calculated for the standard positions from these regressions typically are on the order of ± 0.1% or less, and Monte Carlo simulations of the uncertainties of the predicted *J*'s are also less than ± 0.1%. However, in recognition of the subtle difficulties of assessing flux

gradients, a more conservative ± 0.2% 1σ uncertainty in J is arbitrarily assigned to all unknowns.

$^{40}Ar/^{39}Ar$ extractions were performed using a focused CO_2 laser to quickly fuse individual feldspar crystals and liberate trapped argon. Gasses were exposed for several minutes to an approximately −130 °C cryosurface to trap H_2O and to SAES getters to remove reactive compounds (CO, CO_2, N_2, O_2 and H_2). This was followed immediately by measurement of five argon isotopes on a MAP 215-50 mass spectrometer for approximately 30 min. From 9 to 45 grains were analyzed per sample, totaling 324 single-crystal age determinations. Further details of the dating methodology are given in Deino and Potts [83], Best et al. [82] and Deino et al. [84].

Age-probability density spectra illustrate that most samples exhibit unimodal distributions of single-crystal ages (Fig. 6). These distributions have occasional, obvious age outliers, identified as those analyses yielding ages greater than 0.5 Ma from the median. These outliers are either magmatic xenocrysts, detrital contaminants or contain excess argon, and were eliminated from five samples (45 grains total; these statistics exclude sample BARS/94-10 which was excluded entirely). Most crystals exhibited high relative proportions of radiogenic ^{40}Ar to total ^{40}Ar; however, in an effort to mitigate the effects of subtle alteration implied by relatively low radiogenic yields, 14 grains falling below the arbitrary cutoff of 80% were eliminated. Finally, a robust outlier deletion approach using a measure of normalized deviations from the median (1.9 nMads from the median) identified 19 grains that were omitted from further analysis. All but one of these was older than the median, possibly due to variable amounts of excess ^{40}Ar. A final single analysis was excluded as a bad spectrometer run. The results are fairly robust to the data-reduction procedure; apart from removal of the 'obvious outliers', this culling process affected overall unit ages by no more than 0.2%.

Appendix C. Supplementary data

Supplementary data associated with this article can be found, in the online version, at doi:10.1016/j.epsl.2006.04.009.

References

[1] M.H. Trauth, M.A. Maslin, A. Deino, M.R. Strecker, Late Cenozoic moisture history of East Africa, Science 309 (2005) 2051–2053.

[2] N.E. Levin, J. Quade, S.W. Simpson, S. Semaw, M. Rogers, Isotopic evidence for Plio-Pleistocene environmental change at Gona, Ethiopia, Earth Planet. Sci. Lett. 219 (2004) 93–110.

[3] P.B. deMenocal, African climate change and faunal evolution during the Pliocene–Pleistocene, Earth Planet. Sci. Lett. 220 (2004) 3–24.

[4] P.B. deMenocal, J. Bloemendal, Plio-Pleistocene climatic variability in subtropical Africa and the paleoenvrionment of hominid evolution, in: E.S. Vrba, G.H. Denton, T.C. Partridge, L.H. Burckle (Eds.), Paleoclimate and Evolution, with Emphasis on Human Origins, Yale University Press, New Haven, 1995, pp. 262–288.

[5] G.H. Haug, R. Tiedemann, Effect of the formation of the Isthmus of Panama on Atlantic Ocean thermohaline circulation, Nature 393 (1998) 673–676.

[6] M.A. Maslin, X.S. Li, M.F. Loutre, A. Berger, The contribution of orbital forcing to the progressive intensification of northern hemisphere glaciation, Quat. Sci. Rev. 17 (1998) 426–441.

[7] F. Gradstein, J. Ogg, A. Smith, A geologic time scale 2004, University Press, Cambridge, 2004, 611 pp.

[8] A.C. Ravelo, D.H. Andreasen, M. Lyle, A. Olivarez Lyle, M.W. Wara, Regional climate shifts caused by gradual global cooling in the Pliocene epoch, Nature 429 (2004) 263.

[9] W.H. Berger, E. Jansen, Mid-Pleistocene climate shift; the Nansen connection, Geophys. Monogr. 85 (1994) 295–311.

[10] M. Mudelsee, K. Stattegger, Exploring the structure of the mid-Pleistocene revolution with advanced methods of time-series analysis, Geol. Rundsch. 86 (1997) 499–511.

[11] G.J.H. McCall, B.H. Baker, J. Walsh, Late Tertiary and Quaternary sediments of the Kenya Rift Valley, in: W.W. Bishop, J.D. Clark (Eds.), Background to Evolution in Africa, Chicago University, Chicago, 1967, pp. 191–220.

[12] G.R. Chapman, S.J. Lippard, J.E. Martyn, The stratigraphy and structure of the Kamasia Range, Kenya Rift Valley, J. Geol. Soc. (Lond.) 135 (1978) 265–281.

[13] L.A.J. Williams, G.R. Chapman, Relationships between major structures, salic volcanism and sedimentation in the Kenya Rift from the equator northwards to Lake Turkana, in: L.E. Frostick, et al., (Eds.), Sedimentation in the African Rifts, Geological Society Special Publication, vol. 25, 1986, pp. 59–74.

[14] A. Hill, G. Curtis, R. Drake, Sedimentary stratigraphy of the Tugen Hills, in: L.E. Frostick, et al., (Eds.), Sedimentation in the African Rifts, . Geological Society Special Publication, vol. 25, 1986, pp. 285–295.

[15] M. Pickford, Late Miocene sediments and fossils from the northern Kenya Rift Valley, Nature 256 (1975) 279–284.

[16] J. Martyn, Pleistocene deposits and new fossil localities in Kenya, Nature 215 (1967) 476–480.

[17] A.L. Deino, L. Tauxe, M. Monaghan, A. Hill, $^{40}Ar/^{39}Ar$ geochronology and paleomagnetic stratigraphy of the Lukeino and lower Chemeron Formations at Tabarin and Kapcheberek, Tugen Hills, Kenya, J. Hum. Evol. 42 (2002) 117–140.

[18] A.L. Deino, A. Hill, $^{40}Ar/^{39}Ar$ dating of Chemeron Formation strata encompassing the site of hominid KNM-BC 1, Tugen Hills, Kenya, J. Hum. Evol. 42 (2002) 141–151.

[19] A. Hill, S. Ward, A.L. Deino, G.H. Curtis, R. Drake, Earliest *Homo*, Nature 355 (1992) 719–722.

[20] G.R. Chapman, M. Brook, Chronostratigraphy of the Baringo Basin, Kenya, in: W.W. Bishop (Ed.), Geological Background to Fossil Man, Scottish Academic Press, London, 1978, pp. 207–223.

[21] A. Hill, R. Drake, L. Tauxe, M. Monaghan, J.C. Barry, A.K. Behrensmeyer, G. Curtis, B.F. Jacobs, L. Jacobs, N. Johnson, D.

Pilbeam, Neogene palaeontology and geochronology of the Baringo Basin, Kenya, J. Hum. Evol. 14 (1985) 759–773.
[22] J. Hilton, A conceptual framework for predicting the occurrence of sediment focusing and sediment redistribution in small lakes, Limnol. Oceanogr. 31 (1985) 1169–1181.
[23] R.J. Sherwood, S.C. Ward, A. Hill, The taxonomic status of the Chemeron temporal (KNM-BC 1), J. Hum. Evol. 42 (2002) 153–184.
[24] S.E. Nicholson, A review of climate dynamics and climate variability in eastern Africa, in: T.C. Johnson, E.O. Odada (Eds.), The Limnology, Climatology and Paleoclimatology of the East African Lakes, Gordon and Breach Publishers, Amsterdam, 1996, pp. 25–56.
[25] S.E. Nicholson, The nature of rainfall variability over Africa on time scales of decades to millenia, Glob. Planet. Change 26 (2000) 137–158.
[26] P.B. deMenocal, D. Rind, Sensitivity of subtropical African and Asian climate to prescribed boundary condition changes: model implications for the Plio-Pleistocene evolution of low-latitude climate, in: T.C. Johnson, E.O. Odada (Eds.), The Limnology, Climatology and Paleoclimatology of the East African Lakes, Gordon and Breach Publishers, Amsterdam, 1996, pp. 57–77.
[27] P.B. deMenocal, African climate change and faunal evolution during the Pliocene–Pliestocene, Earth Planet. Sci. Lett. 220 (2004) 3–24.
[28] J.E. Kutzbach, F.A. Street-Perrott, Milankovitch forcing of fluctuations in the level of tropical lakes from 18 to 0 kyr BP, Nature 317 (1985) 130–134.
[29] E.M. Pokras, A.C. Mix, Earth's precession cycle and Quaternary climatic change in tropical Africa, Nature 326 (1987) 486–487.
[30] A.C. Clement, A. Hall, A.J. Broccoli, The importance of precessional signals in the tropical climate, Clim. Dyn. 22 (2004) 327–341.
[31] S.M. Denison, M.A. Maslin, C. Boot, R.D. Pancost, V.J. Ettwein, Precession-forced changes in south west African vegetation during marine isotope stages 101–100 (approximately 2.56–2.51 Ma), Palaeogeogr. Palaeoclimatol. Palaeoecol. 220 (2005) 375–386.
[32] M. Rossignol-Strick, Mediterranean Quaternary sapropels, an immediate response of the African monsoon to variation of insolation, Palaeogeogr. Palaeoclimatol. Palaeoecol. 49 (1985) 237–263.
[33] F.J. Hilgen, Astronomical calibration of Gauss to Matuyama sapropels in the Mediterranean and implication for the Geomagnetic Polarity Time Scale, Earth Planet. Sci. Lett. 104 (1991) 226–244.
[34] L.J. Lourens, A. Antonarakou, F.J. Hilgen, A.A.M. Van Hoof, C. Vergnaud-Grazzini, W.J. Zachariasse, Evaluation of the Plio-Pleistocene astronomical timescale, Paleoceanography 11 (1996) 391–413.
[35] W.F. Ruddiman, Earth's Climate: Past and Future, W.H. Freeman and Company, New York, 2001, 465 pp.
[36] M.H. Trauth, A.L. Deino, A.G.N. Bergner, M.R. Strecker, East African climate change and orbital forcing during the last 175 kyr BP, Earth Planet. Sci. Lett. 206 (2003) 297–313.
[37] A.G.N. Bergner, M.H. Trauth, B. Bookhagen, Paleoprecipitation estimates for the Lake Naivasha Basin (Kenya) during the last 175 k.y. using a lake-balance model, Glob. Planet. Change 36 (2003) 117–136.
[38] J. Laskar, P. Robutel, F. Joutel, M. Gastineau, A. Correia, B. Levard, A long-term numerical solution for the insolation quantities of the earth, Astron. Astrophys. 428 (2004).
[39] J.L. Kirschvink, The least-squares line and plane and the analysis of palaeomagnetic data, Geophys. J. R. Astron. Soc. 62 (1980) 699–718.
[40] R.A. Fisher, Dispersion on a sphere, Proc. R. Soc. Lond. 217A (1953) 295–305.
[41] P.L. McFadden, M.W. McElhinny, The combined analysis of remagnetization circles and direct observations in palaeomagnetism, Earth Planet. Sci. Lett. 87 (1988) 161–172.
[42] J.C. Stager, B. Cummings, L. Meeker, A high-resolution 11,400-yr diatom record from Lake Victoria, East Africa, Quat. Res. 47 (1997) 172–181.
[43] R.E. Hecky, H.J. Kling, Phytoplankton ecology of the great lakes of the rift valleys of central Africa, Arch. Hydrobiol. Beheifte Ergeb. Limnol. 25 (1987) 197–228.
[44] F. Gasse, Les Diatomées lacustres Plio-Pléistocenes du Gadeb (Éthiopie): Systématique, paléoécologie, biostratigrahie, Rev. Algol., Mém 3 (1980).
[45] J.C. Stager, B.F. Cumming, L.D. Meeker, A 10,000-year high resolution diatom record of Pilkington Bay, Lake Victoria, East Africa, Quat. Res. 59 (2003) 172–181.
[46] F. Gasse, P. Barker, T.C. Johnson, A 24,000 yr diatom record from the northern basin of Lake Malawi, in: E. Odada, D.O. Olago (Eds.), The East African Great Lakes: Limnology, Paleolimnology and Biodiversity, Kluwer, 2002, pp. 393–414.
[47] R.B. Owen, R. Crossley, Spatial and temporal distribution of diatoms in sediments of Lake Malawi, central Africa, and ecological implications, J. Paleolimnol. 7 (1992) 55–71.
[48] F. Gasse, D.F. Talling, P. Kilham, Diatom assemblages in East Africa: classification, distribution and ecology, Rev. Hydrobiol. Trop. 16 (1983) 3–34.
[49] C.H. Pilskahn, Seasonal and interannual particle export in an African Rift Valley Lake: a -yr record from Lake Malawi, southern East Africa, Limnol. Oceanogr. 49 (2004) 964–977.
[50] J. Kingston, A.L. Deino, R.K. Edgar, A. Hill, Astronomically forced climate change in the Kenyan Rift Valley 2.7–2.55 Ma: implications for the evolution of early hominin ecosystems, J. Hum. Evol. (in press).
[51] J.C. Stager, Ancient analogues for recent environmental changes at Lake Victoria, East Africa, Monogr. Biol. 79 (1998) 37–46.
[52] L.E. Lisiecki, M.E. Raymo, A Pliocene–Pliestocene stack of 57 globally distributed benthic $\delta^{18}O$ records, Paleoceanography 20 (2005) PA1003.
[53] A.L. Deino, R. Potts, Single-crystal $^{40}Ar/^{39}Ar$ dating of the Olorgesailie Formation, southern Kenya Rift, J. Geophys. Res. B, Solid Earth Planets 95 (1990) 8453–8470.
[54] R. Mundil, K.R. Ludwig, I. Metcalfe, P.R. Renne, Age and timing of the Permian mass extinctions: U/Pb dating of closed-system zircons, Science 305 (2004) 1760–1763.
[55] K. Min, R. Mundil, P.R. Renne, K.R. Ludwig, A test for systematic errors in $^{40}Ar/^{39}Ar$ geochronology through comparison with U/Pb analysis of a 1.1-Ga rhyolite, Geochim. Cosmochim. Acta 64 (2000) 73–98.
[56] K. Kuiper, Direct intercalibration of radio-isotopic and astronomical time in the Mediterranean Neogene, Geol. Ultraiectina 235 (2003) 147–165.
[57] K.F. Kuiper, F.J. Hilgen, J. Steenbrink, J.R. Wijbrans, Ar-40/Ar-39 ages of tephras intercalated in astronomically tuned Neogene sedimentary sequences in the eastern Mediterranean, Earth Planet. Sci. Lett. 222 (2004) 583–597.
[58] M.A.J. Williams, F.M. Williams, F. Gasse, G.H. Curtis, D.A. Adamson, Plio-Pleistocene environments at Gadeb prehistoric site, Ethiopia, Nature 282 (1979) 29–33.

[59] K.E.K. St. John, Evidence that's an ocean apart: co-varying records of ice-rafted debris flux and Plio-Pleistocene bipolar ice sheet disintegration, Sediment. Rec. 2 (2004) 4–8.
[60] S. Clemens, W.L. Prell, D. Murray, G.B. Shimmield, G.P. Weedon, Forcing mechanisms of the Indian Ocean monsoon, Nature 353 (1991) 720–725.
[61] M.A. Cane, P. Molnar, Closing of the Indonesian seaway as a precursor to East African aridification around 3–4 million years ago, Nature 411 (2001) 157–162.
[62] S. Semaw, M.J. Rogers, J. Quade, P.R. Renne, R.F. Butler, M. Dominguez-Rodfigo, D. Stout, W.S. Hart, T. Pickering, S. Simpsonj, 2.6-Million-year-old stone tools and associated bones from OGS-6 and OGS-7, Gona, Afar, Ethiopia, J. Hum. Evol. 45 (2003) 169–177.
[63] B. Asfaw, T. White, O. Lovejoy, B. Latimer, S. Simpson, G. Suwa, Australopithecus garhi: a new species of early hominid from Ethiopia, Science 284 (1999) 629–635.
[64] R.L. Holloway, Brain, in: E. Delson, I. Tattersall, J.V. Couvering, A.S. Brooks (Eds.), Encyclopedia of Human Evolution and Prehistory, Garland Publishing, Inc., New York, 2000, pp. 141–149.
[65] B.G. Richmond, L.C. Aiello, B.A. Wood, Early hominin limb proportions, J. Hum. Evol. 43 (2002) 529–548.
[66] L. Gabunia, S.C. Anton, D. Lordkipanidze, A. Vekua, A. Justus, C.C. Swisher III, Dmanisi and dispersal, Evol. Anthropol. 10 (2001) 158–170.
[67] B. Wood, Origin and evolution of the genus *Homo*, Nature 355 (1992) 783–790.
[68] B.A. Wood, B.J. Richmond, Human evolution: taxonomy and paleobiology, J. Anat. 196 (2000) 19–60.
[69] G. Suwa, T.D. White, F.C. Howell, Mandibular postcanine dentition from the Shungura Formation, Ethiopia: crown morphology, taxonomic allocations, and Plio-Pleistocene hominid evolution, Am. J. Phys. Anthropol. 101 (1996) 247–282.
[70] B. Wood, M. Collard, The changing face of genus *Homo*, Evol. Anthropol. 8 (1999) 195–207.
[71] I. Tattersall, J.H. Schwartz, Extinct Humans, Westview, Boulder, CO, 2000.
[72] E.S. Vrba, On the connections between paleoclimate and evolution, in: E.S. Vrba, G.H. Denton, T.C. Partridge, L.H. Burckle (Eds.), Paleoclimate and evolution, with emphasis on human origins, Yale University Press, New Haven, 1995, pp. 24–45.
[73] T.G. Bromage, F. Schrenk, African Biogeography, Climate Change, and Human Evolution, Oxford University Press, New York, 1999.
[74] C.S. Feibel, Debating the environmental factors in hominid evolution, GSA Today 7 (1997) 1–7.
[75] R.L. Hay, Geology of the Olduvai Gorge, University of California Press, Berkeley, 1976.
[76] R. Potts, A.K. Behrensmeyer, P. Ditchfield, Paleolandscape variation and early Pleistocene hominid activities: Members 1 and 7, Olorgesailie Formation, Kenya, J. Hum. Evol. 37 (1999) 747–788.
[77] R. Bonnefille, R. Potts, F. Chalie, D. Jolly, O. Peyron, High-resolution vegetation and climate change associated with Pliocene *Australopithecus afarensis*, Proc. Natl. Acad. Sci. 101 (2004) 12125–12129.
[78] C.S. Feibel, F.H. Brown, I. McDougall, Stratigraphic context of fossil hominids from the Omo Group deposits: northern Turkana Basin, Kenya and Ethiopia, Am. J. Phys. Anthropol. 78 (1989) 595–622.
[79] N. Silverman, B. Richmond, B. Wood, Testing the taxonomic integrity of *Paranthropus boisei* sensu stricto, Am. J. Phys. Anthropol. 115 (2001) 167–178.
[80] B.B. Ellwood, W.D. MacDonald, J.A. Wolff, The slot technique for rock magnetic sampling, Phys. Earth Planet. Inter. 78 (1993) 51–56.
[81] P.R. Renne, C.C. Swisher, A.L. Deino, D.B. Karner, T.L. Owens, D.J. DePaolo, Intercalibration of standards, absolute ages and uncertainties in $^{40}Ar/^{39}Ar$ dating, Chem. Geol. 145 (1998) 117–152.
[82] M.G. Best, E.H. Christiansen, A.L. Deino, C.S. Gromme, D.G. Tingey, Correlation and emplacement of a large, zoned, discontinuously exposed ash flow sheet; the $^{40}Ar/^{39}Ar$ chronology, paleomagnetism, and petrology of the Pahranagat Formation, Nevada, J. Geophys. Res. B, Solid Earth Planets 100 (1995) 24,593–524,609.
[83] A.L. Deino, R. Potts, Single-crystal$^{40}Ar/^{39}Ar$ dating of the Olorgesailie Formation, southern Kenya Rift, J. Geophys. Res. B, Solid Earth Planets 95 (1990) 8453–8470.
[84] A.L. Deino, P.R. Renne, C.C.I. Swisher, $^{40}Ar/^{39}Ar$ dating in paleoanthropology and archaeology, Evol. Anthropol. 6 (1998) 63–75.